

# High sensitivity electrochemical DNA sensors for detection of somatic mutations in FFPE samples

Valentina Egorova\*

*Belarusian State Pedagogical University, Minsk, Belarus*

Halina Grushevskaya†

*Physics Faculty, Belarusian State University, 4 Nezavisimosti Ave., 220030 Minsk, Belarus*

Nina Krylova‡

*Belarusian State Agrarian Technical University, Minsk, Belarus*

Igor Lipnevich§

*Belarusian State University, Minsk, Belarus*

Egor Vaskovtsev¶

*Belarusian State Pedagogical University, Minsk, The Republic of Belarus*

Andrei Babenka\*\*

*Belarusian State Medical University, Minsk, Belarus*

Ina Anufreyonak†† and Siarhei Smirnov‡‡

*N. N. Alexandrov National Cancer Center of Belarus, Lesnoy, Belarus*

We offer new high-performance label-free electrochemical impedimetric DNA sensors of non-faradaic type. The DNA sensors based on a platform of crystalline carbon nanotube (CNT) arrays are fabricated by the Langmuir–Blodgett (LB) deposition technique. The CNT arrays are suspended on a nanoporous anodic alumina (aluminium oxide, AOA) support. Single-stranded (ss) 19- and 20-base oligonucleotides and double-stranded (ds) nucleotide sequences were used as probes for chosen molecular target – human KRAS (Kirsten Rat Sarcoma viral oncogene homolog) gene. Genomic deoxyribonucleic acids (DNAs) were isolated from placenta of healthy donors and FFPE (formalin-fixed, paraffinembedded) samples of tumor tissue. Raman spectral analysis and electrochemical dielectric spectroscopy were used to sequence the target DNAs. The optical and electrochemical detection (variants of DNA sequencing) were based on a screening effect that grows after the DNA homoduplex formation. We demonstrated that such technologies are very sensitive and allow to detect attomolar DNA concentrations and less. As result, the KRAS exon 2, codon 12, c.35G>A mutation was successfully discriminated in human genomic DNA isolated from FFPE colorectal cancer tumor tissue samples.

**Keywords:** DNA-carbon nanotube hybrid, conducting polymer, electric-field screening effect, temperature effects, DNA melting, attomolar DNA sensor, diagnostics

## I. INTRODUCTION

The modern approaches to tumor therapy cannot exist without high-quality molecular diagnostics. Currently, the U.S. Food and Drug Administration (FDA) has approved dozens of molecular tests aimed at choosing targeted therapy for tumors of various nosological forms: colorectal cancer, breast cancer, lung cancer, etc. [1–3] Most often, FFPE sections are used for solid tumors. This allows the operator to select the area of interest for analysis as accurately

---

\*Electronic address: egorova`vp@bspu.by

†Electronic address: grushevskaja@bsu.by

‡Electronic address: nina-kr@tut.by

§Electronic address: lipnevich@bsu.by

¶Electronic address: vaskovcev@mail.ru

\*\*Electronic address: labmdbt@gmail.com

††Electronic address: klaksa`06@mail.ru

‡‡Electronic address: rustledeath24@gmail.com

as possible [4]. The quality of the extracted DNA varies greatly from sample to sample. This has a strong influence on the results of molecular tests [5]. During the preparation of FFPE blocks, the DNA undergoes fragmentation. As a result, the number of sites for annealing of oligonucleotide primers is reduced. This is a key parameter for the implementation of PCR-based techniques. When extracting and purifying DNA from FFPE sections, the degree of fragmentation also increases, further reducing sample quality. In addition, the effectiveness of PCR-based methods is also affected by the presence of inhibitors that enter the DNA solution in small concentrations. This may not stop the reaction, but reduce its effectiveness. When there are very few target sequences in solution, this can be crucial and lead to diagnostic errors [6]. One possible solution to the problem is the use of DNA sensors and electrochemical impedance spectroscopy (EIS). Since this is not a standard approach, it has many directions and mechanisms [7]. DNA sensors have at least two advantages. First, they are much less dependent on the presence of inhibitors in the DNA sample compared to methods using enzymes. Second, a shorter DNA fragment/probe is used to recognize the target sequence. This increases the number of fragmented DNA sequences suitable for recognition [8]. Currently, there are no ready-made solutions that would fully meet the needs of the clinical diagnostics market. Many DNA sensor technologies have a number of disadvantages so far. Their improvement and optimization for work in real clinical conditions is an important and priority area of research [9, 10]. To date, the development of low-temperature genotyping also is in high demand [11].

Graphene materials and, in particularly, rolled atomically-thin carbon layers called carbon nanotubes are promising materials for development of high performance electrochemical and optical transducers of DNA-hybridization signals. The transducers operating on plasmon resonance effects in the nanomaterials are capable to perform the nucleotide sequencing of samples with ultralow DNA-target concentrations: attomoles and less [12]. Massless graphene charge carriers are high mobile even in comparison with electrons of the ordinary metals. Physics of the graphene charge carriers residing in valleys  $K, K'$  of graphene Brillouin zone is Dirac physics. Chirality of the massless pseudo Dirac fermions prevents annihilation of electron-hole pairs. But, the charge transport in graphene also is featured by signs of a non-Abelian statistics of the Majorana quasiparticles with a nontrivial topology [13–18].

However, the electrical and optical properties of nanostructured graphene-like materials strongly depend on accidental environmental impurities that leads to wide spread of characteristics of the graphene-based devices. Moreover, when scattering and obliquely tunneling through the environmental defects the graphene charge carriers can be confined as Klein resonances [19]. The electrostatical confinement is predicted within the topologically-nontrivial graphene model [20]. The fine tuning of the Klein resonances is a challenge. To design a graphene-based material with specified characteristics one needs the Langmuir–Blodgett technique which allows to fabricate highly ordering defect-free layered nanocomposites which include few-walled carbon nanotubes (FWCNTs).

Immobilization of DNA on the graphene surface or using of high-conductive oligomer improve electrical transport along DNA (see [21–24] and references therein). But, the specificity of the probe DNA is attenuated at its immobilization. Therefore, the construction of impurity-insensitive label-free PCR-free transducers based on graphene materials for detection of single-molecule hybridization signal is complicated and unsolved problem.

The homoduplex formation can be indicated through emerging transition from the fully ordered double-helix state of ssDNA probe–ssDNA target duplexes to the metastable state of the complexes at the temperature increase. Although the extended linear conformation of the probe and target ssDNA molecules entering the homoduplex remains in the metastable state, the molecules separate from each other in a diffusion process because they are not linked by hydrogen bonds and, correspondingly, almost do not interact with each other. As a result, a helix-coil transition happens at the temperature alternation. The melting of long dsDNA at temperature increase is a phase transition of the first order [25]. The temperature of the DNA transition (so-called melting temperature  $T_m$ ) from the helicoidal form to the linear one depends on the length of the ssDNA molecules. The phase transitions at DNA melting are detected in a wide temperature region because  $T_m$  depends significantly on the oligonucleotide length and base composition. Developing DNA sequencing methods one needs to narrow the temperature region. The value of  $T_m$  is also necessary to design the DNA probes as its experimental determination reduces the time needed for construction of DNA probes with required parameters.

When creating a network the complexification between highly-ordered carbon-nanotube arrays and dsDNA target molecules do not impair but improve the ability of the FWCNT arrays to screen electric fields [26, 27]. The high-conductive oligomers with conjugated double bonds and FWCNTs form a network also, enhancing the efficiency of the screening by the highly-ordered FWCNT arrays [28, 29].

In the paper we intend to discriminate a mutation status of KRAS gene. When activated, a KRAS protein is involved in the dephosphorylation of guanosine triphosphate (GTP) to guanosine diphosphate (GDP), after which KRAS is turned off. KRAS-gene single base mutations called single-oligonucleotide polymorphisms (SNPs) most often occur in exon 2, codon 12 of the KRAS gene with the nucleotide change c.35G>A (substitution, position 35, G→A) resulting in the amino acid change p.G12D (substitution – missense, position 12, Gly12Asp (G→D)) We offer to detect the genotype on a change of the degree of shielding by a sensor electrode coating in a result of the DNA homoduplex formation on the FWCNT which surface was decorated by conducting oligomers of thiophene-pyrrole

series entering cyclic organometallic complexes. The screening efficiency for the network created by linkage of hybrids between the homoduplexes and decorated CNTs grows but a transfer of electrons along the organometallic complexes is broken because when penetrating through nanocavities of the nanocyclic compound the target DNA disturbs perfect location of S atoms in the thiophene groups relative to the nitrogen atoms of the pyrrole groups [26, 29]. We shall elucidate the origin of light-scattering enhancement for dsDNA deposited on the graphene plane as a result of intensive graphene-charge-density oscillations in resonance with vibrations of the dsDNA molecular groups, which are distant enough from the graphene surface. We shall experimentally show that the light scattering in the dsDNA homoduplexes deposited on rolled graphene monolayers is enhanced by graphene charge carriers of the pseudo-Majorana type rather than the pseudo-Dirac type ones.

A goal of the paper is to develop a high-performance low-temperature PCR-free electrochemical sensor for KRAS c.35G>A, p.G12D genotyping in FFPE tumor samples. The sensor operates on screening near-electrode double layer by crystalline FWCNT arrays. We shall show that depositing oligonucleotides of several types on the electrode surface one gets an EIS DNA chip for discriminating between two alleles of KRAS-oncogene. The KRAS-oncogene sequencing will be verified by a DNA-melting control.

## II. MATERIALS AND METHODS

### A. Reagents

Genotyping was performed in placental DNA, nuclear DNA of C6-line rat glioma cells, and tumor DNA denoted by dsDNA<sub>pl</sub>, dsDNA<sub>C6</sub>, and dsDNA<sub>CRC</sub>, respectively. The following SNP: c.35G>A site, p.G12D, located in the second exon of the human KRAS gene (NCBI/Gene KRAS genomic DNA sequence NC\_000012.12; NCBI/Gene KRAS mRNA var d sequence NM\_001369787.1), was used as a molecular target. Clinical samples were collected at the N. N. Alexandrov National Cancer Center of Belarus. The study included 10 FFPE samples obtained from patients with advanced colon cancer. For isolation, 2–3 sections of the paraffin block were used. Deparaffinization was performed with xylene followed by washing with ethanol (95%). Total DNA isolation was performed using the QIAamp DNA FFPE Tissue Kit (Qiagen) according to the manufacturer's protocol.

The C6-line rat glioma cells were cultured in standard conditions. The native dsDNA<sub>pl</sub> was isolated from placenta tissue of healthy donors. RNA and proteins contents in the high purity dsDNA<sub>pl</sub> and dsDNA<sub>C6</sub> (1.03 mg/ml in 10<sup>-5</sup> M Na<sub>2</sub>CO<sub>3</sub> buffer medium) were less than 0.1 % (optical density ratio  $D_{260}/D_{230} = 2.378$  and  $D_{260}/D_{280} = 1.866$ , respectively).

The single stranded 19- and 20-base oligonucleotides, short primers KRAS<sub>w</sub> and KRAS<sub>m</sub>, and two double-stranded (toehold exchange) probes, P3/W3 and ssDNA<sub>lp</sub>/ssDNA<sub>Wm</sub>, were utilized as DNA probes (see Table I). The perfect-matched (KRAS<sub>w</sub>) and single-mismatched (KRAS<sub>m</sub>) probes are complementary to the KRAS-gene wild-type (non-mutant) and mutant-type nucleotide sequences, respectively. The P3/W3 toehold duplex consisted of the two 35-base and 28-base oligonucleotides. The longer capture oligonucleotide, W3, is complementary to the wild KRAS gene. The four inosines replace guanines in the shorter chain, P3, being a protector of the capture oligonucleotide "W3". The ssDNA<sub>lp</sub>/ssDNA<sub>Wm</sub> toehold duplex consisted of the two 47-base and 40-base oligonucleotides. The longer capture oligonucleotide, ssDNA<sub>Wm</sub>, is complementary to the KRAS gene with the SNP. The five inosines replace guanines in the shorter chain, ssDNA<sub>lp</sub>, being a protector of the capture oligonucleotide, ssDNA<sub>Wm</sub>.

The toehold exchange probes were fabricated by annealing the protector P3 or ssDNA<sub>lp</sub> strands mixed in the ratio 2:1 with the complementary W3 or ssDNA<sub>Wm</sub> strands, respectively, in TE buffer at 37 ± 0.1 °C. The 35-base oligonucleotides denoted by "N3" and "M3" in Table I are the perfect-matched and single-base mismatched KRAS-gene sequences and have been used as wild- and mutant-type model target ssDNAs, respectively. The 47-base oligonucleotide denoted by "DNA<sub>lm</sub>" in Table I is the single-base mismatched KRAS-gene sequence and has been used as mutant-type model target ssDNA.

A DNA chip was fabricated with the two oligonucleotides: KRAS<sub>m</sub> and P3/W3, or P3/W3 and 25-base guanine oligonucleotide (polyG), or KRAS<sub>w</sub> and ssDNA<sub>lp</sub>/ssDNA<sub>Wm</sub>. The hybridization reaction lasted 30 minutes. All DNA probes were purchased from "Primetech ALC" (Minsk, Belarus).

The carboxylated and stearic-acid-functionalized FWCNTs under 2.5 nm in diameter have been decorated by the cyclic complexes (Fe(II)DTP) of Ce and/or high-spin octahedral Fe(II) with 3-hexadecyl-2,5-di(2-thienyl)-1H-pyrrole (H-DTP, H-dithienylpyrrole) ligands [30]. The H-DTP is an amphiphilic conducting oligomer of thiophene-pyrrole derivatives. An alkyl 16-link hydrocarbon chain  $R = C_{16}H_{33}$  was chemically bounded to the oligomer. Inverse micelles of stearic acid with FWCNTs, or DNA-FWCNT, or DNA inside (called micellar FWCNTs, micellar DNA-FWCNT hybrids, and micellar DNA) are obtained by mixing stearic acid and the appropriate reagent dissolved in hexane by the ultrasound treatment.

Salts Fe(NO<sub>3</sub>)<sub>3</sub> · 9H<sub>2</sub>O, Ce<sub>2</sub>(SO<sub>4</sub>)<sub>3</sub> (Sigma, USA), hydrochloric acid, deionized water with resistivity of

TABLE I: Sequences of all the oligonucleotides used in this study.

Name	Sequence structure ( $5' \rightarrow 3'$ )
N <sub>3</sub>	TGGTGGCGTAGGCAAGAGTGCCTTGACGATACAGC
P <sub>3</sub>	GCTGTATCGTCAAGGCACTCTTGCCTACGCCACCA
W <sub>3</sub>	TGGTGICGTAGICAAGAITGCCTTIACG
M <sub>3</sub>	TGA <b>T</b> TGGCGTAGGCAAGAGTGCCTTGACGATACAGC
KRAS <sub>w</sub>	GTTGGAGCTGGTGGCGTAG
KRAS <sub>m</sub>	AGTTGGAGCTGA <b>T</b> TGGCGTAG
ssDNA <sub>lp</sub>	AATAAGGAGGCACTCTTGCCTACGCCATCAGCTCCAACTACCACAAG
ssDNA <sub>wm</sub>	CTTGTGITAGTTGGAGCTGATGICGTAGICAAIAGTICTT
ssDNA <sub>lm</sub>	CTTGTGGTAGTTGGAGCTGA <b>T</b> TGGCGTAGGCAAGAGTGCCTCCTTATT
polyG	GGGGGGGGGGGGGGGGGGGGGGGGGGGGGG

18.2  $M\Omega\cdot\text{cm}$  were used to prepare subphases. All chemical reagents of analytical grade were used without further purification.

## B. Methods

### 1. Fabrication of dithienylpyrrole-coated FWCNT arrays

By employing the LB technique monomolecular crystalline DNA-FWCNT hybrid layers (DNA-FWCNT hybrid crystalline monolayers) were fabricated by compressing two-dimensional gas of inverse stearic-acid micelles with the carboxylated FWCNTs and DNA probe molecules inside. The hexane solution of the micellar DNA-FWCNT hybrids was preliminary dropped on deionized-water surface. Then the two DNA-FWCNT hybrid LB-monolayers were formed and deposited onto surface of interdigital electrode structures which were isolated by nanoporous AOA, 10-nm pore diameter.

Preliminary, five iron-containing LB-monolayers consisting of the cyclic complex (Fe(II)DTP) of octahedral high spin Fe(II) with DTP ligands were formed. The FWCNTs were decorated by the nanocyclic organometallic LB-complexes. The FWCNT LB-arrays decorated by the dithienylpyrrole complexes of octahedral high spin Fe(II) host spin-polarized graphene charge carriers [31–33].

## 2. Electrochemical impedance measurements

EIS measurements have been made with a BORDO-322 digital oscilloscope (UniTechProm, Minsk, Belarus) which provides automatic measurements and mathematical signal processing (fast Fourier transforms) of harmonic electrical signals.

Interdigital electrode structures deposited on a glass-ceramic support (pyroceramics) are utilized.  $N_e$  pairs,  $N_e = 20$  of the aluminium electrodes are arranged in an Archimedes-type spiral configuration. Every such pair is an “open type” capacitor. To record DNA-hybridization signals a transducer sensitive layer was formed on the surface of the electrode structures in a following way. The oligonucleotide sequences–FWCNT hybrid LB-arrays decorated by the LB-films of the nanocyclic organometallic complexes were deposited on the interdigital structure of aluminium electrodes, on the surface of which the nanoporous anodic alumina layer were previously formed.

To excite harmonic auto-oscillations of electric current (charge–discharge (charging) processes in capacitors), the planar capacitive sensor of interdigital-type was connected as the capacitance,  $C$ , into the relaxation resistance–capacitance (RC) oscillator (self-excited  $RC$ -oscillator) [34]. A self-excitation of an amplifier with a positive feedback occurs in such RC-oscillator on quasi-resonance frequencies. The capacitance  $C$  of the sensor entering the measuring RC-oscillating circuit has been calculated by the formula  $C = 1/(2\pi Rf)$ , where  $f$  is a quasi-resonance frequency.

The Bode plots were recorded in the deionized water.

### 3. DNA detection

Double-stranded DNA was denatured at 95 °C before detection. The denatured DNA was hybridized with a DNA probe.

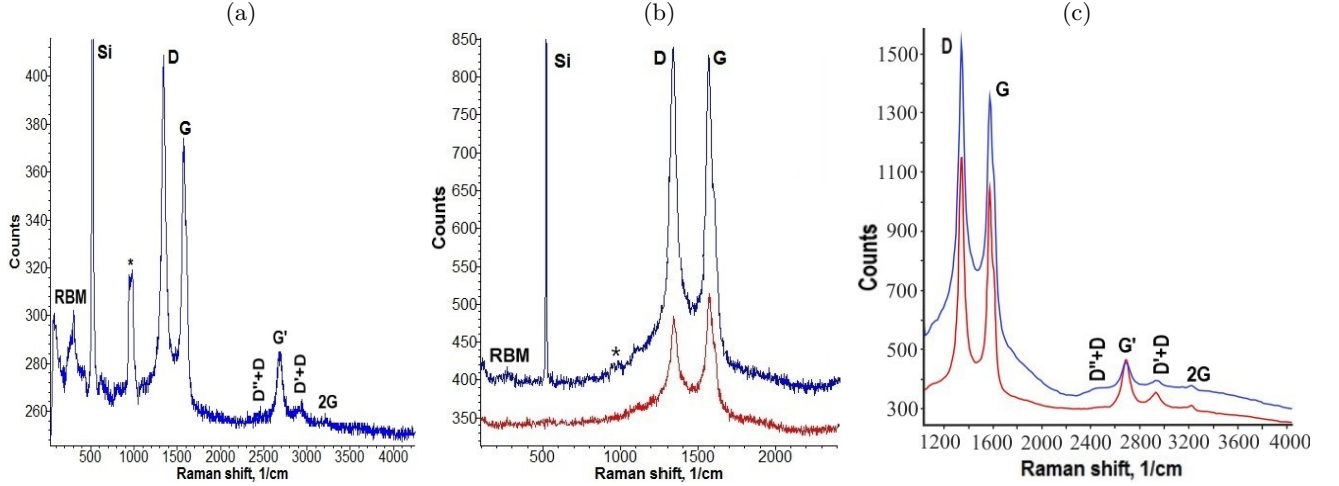


FIG. 1: Raman spectra of (a) the stearic acid micelles with dsDNA<sub>p1</sub>-FWCNTs inside, (b) the micellar KRAS<sub>w</sub>-FWCNTs hybrids (red curve in figure b) and a broken-down (crumpled) LB-monolayer from the stearic acid micelles with KRAS<sub>w</sub>-FWCNTs hybrids inside (blue curve in figure b), (c) the LB-monolayer formed by the micellar dsDNA<sub>p1</sub>-CNT hybrids with (c, blue curve) or without (c, red curve) propidium iodide. The micellar KRAS<sub>w</sub>-FWCNT, dsDNA<sub>p1</sub>-FWCNT hybrids, and the KRAS<sub>w</sub>-FWCNT hybrid LB-monolayer were deposited on pure Si supports; the dsDNA<sub>p1</sub>-CNT hybrid LB-monolayer was deposited on the Si support hydrophilized by H-DTP. The Raman spectra were recorded at laser excitation wavelength of 532 nm; the following laser powers and collected times were used for the specimen excitation: 20 mW and 1 s (figure (a)), 3 mW and 10 s (figures b and c). “\*” denotes a laser mode.

### 4. Raman spectroscopy

Spectral studies in visible range were carried out using a confocal micro-Raman spectrometer Nanofinder HE (“LOTIS-TII”, Tokyo, Japan–Belarus) on lasers operating at wavelengths of 473 (DPSS laser), and 532 (DPSS laser) nm with power in the range from 0.0001 to 20 mW. The spectra were recorded in the back-scattering geometry under a  $\times 50$  objective at room (RT) temperature. The size for the optical image is of  $7 \times 7 \mu\text{m}$ , vertical spatial resolution 150 nm, spectral resolution is of up to 0.01 nm.

## III. CHARACTERIZATION OF CAPACITIVE TRANSDUCER AND PRINCIPLE OF ITS OPERATION

### A. Raman spectral study of DNA–CNT hybrid interactions

A prominent CNT radial breathing mode (RBM) of  $298 \text{ cm}^{-1}$  is featured in Raman spectra of the transducer DNA–CNT hybrid layer (see Figs. 1a and b). Let us estimate the CNTs diameters using the formula [35]

$$\omega_{RBM} = \frac{227}{d_t} \sqrt{1 + C_{env} d_t^2} \quad (\text{III.1})$$

where  $C_{env}$  quantifies the environmental effect on the RBM frequency,  $d_t$  is a diameter of single walled carbon nanotubes (SWCNTs). We estimate approximately the  $C_{env}$  at zero in the case of the isolated original carboxylated few-walled CNTs. The CNT diameter is estimated at 0.761 nm for the RBM of  $298.28 \text{ cm}^{-1}$ . CNTs with such diameter are single-walled ones. Using the following formula [36]:

$$d_t = \frac{0.246}{\pi} \sqrt{(n^2 + nm + m^2)} \quad (\text{III.2})$$

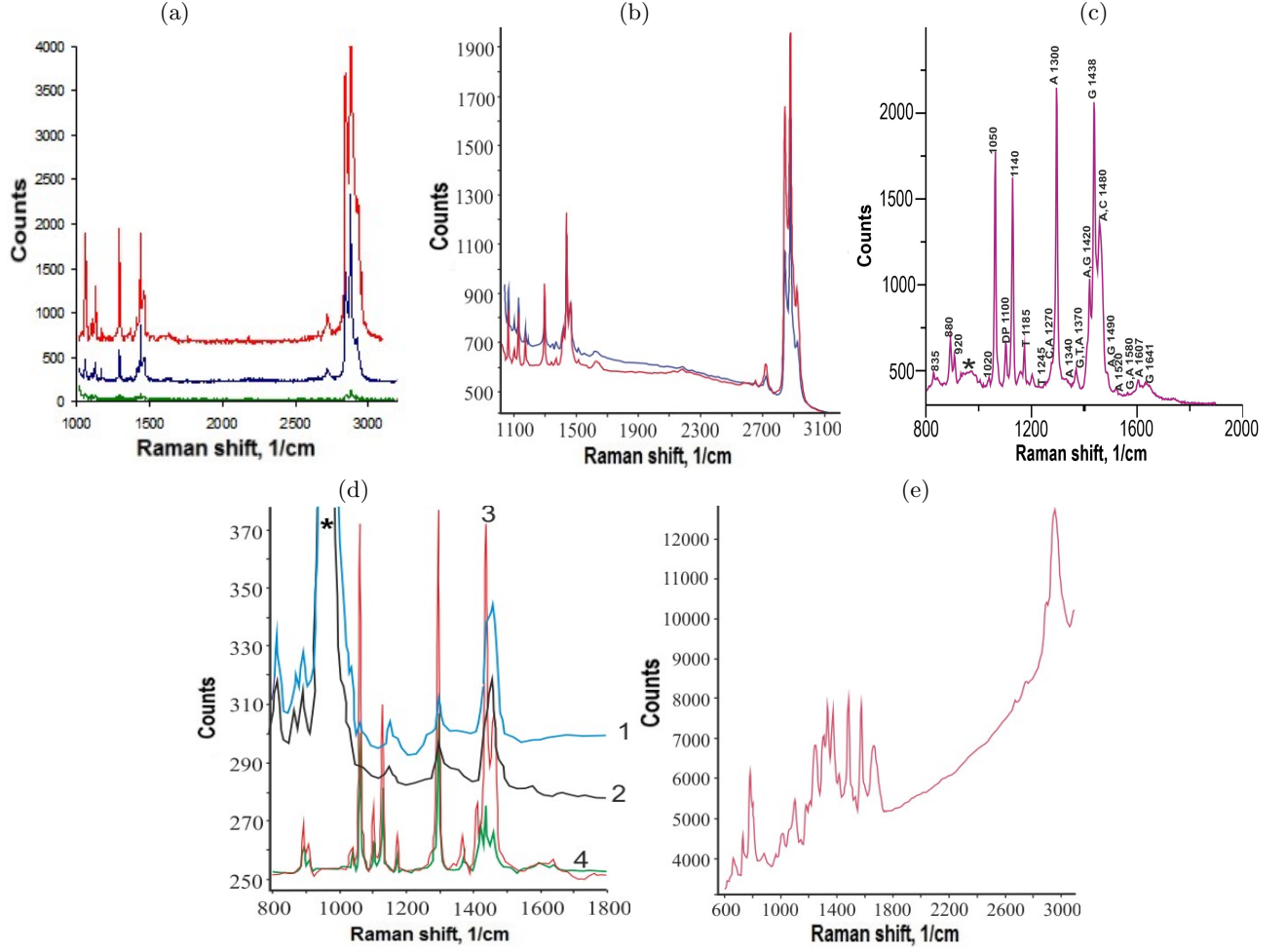


FIG. 2: (a) Raman spectra of pure stearic acid inverse micelles (green curve in figure a), the micelles with  $\text{dsDNA}_{\text{pl}}$  inside (blue curve in figure a), the micelles with  $\text{dsDNA}_{\text{pl}}$ -FWCNTs inside (red curve in figure a); the pure stearic acid micelles and the micelles with  $\text{dsDNA}_{\text{pl}}$  and  $\text{dsDNA}_{\text{pl}}$ -FWCNT hybrids inside were deposited on pure Si supports; the Raman spectra were recorded at laser excitation wavelength of 532 nm; the laser power and collected time were used for the specimen excitation: 2 mW and 60 s, respectively. (b) Raman spectra of the micellar nuclear  $\text{dsDNA}_{\text{C6}}$  (red curve) and the micellar tumor  $\text{dsDNA}_{\text{CRC}}$  (blue curve); the  $\text{dsDNA}_{\text{C6}}$  and the  $\text{dsDNA}_{\text{CRC}}$  were deposited on pure Si supports; the Raman spectra were recorded at laser excitation wavelength of 532 nm; the laser power and collected time were used for the specimen excitation: 2 mW and 60 s. (c) A Raman low-frequency part of the spectrum for the inverse micelles formed in hexane solution of mixture from stearic acid with  $\text{dsDNA}_{\text{pl}}$  and dripped on pure Si. The numbers indicate the characteristic frequencies of dsDNA vibrations; adenine, guanine, thymine and cytosine are designated by A, G, T and C, respectively; DP denotes phosphodiester bond. Laser power, excitation wavelength, and collected time were of 20 mW, 532 nm, and 3 s, respectively. (d) Raman spectra of the micellar  $\text{dsDNA}_{\text{pl}}$  (blue and black curves 1 and 2, respectively) and the micellar  $\text{dsDNA}_{\text{pl}}$ -CNT hybrids (red and green curves 3 and 4, respectively); the micellar  $\text{dsDNA}_{\text{pl}}$  and  $\text{dsDNA}_{\text{pl}}$ -CNT hybrids were deposited on the Si hydrophilized by H-DTP; the Raman spectra were recorded at laser excitation wavelengths of 473 nm (curves 1 and 3) and 532 nm (curves 2 and 4), the following laser powers and collected times were used for the specimen excitation: 8 mW and 1 s (curves 1 and 3), 20 mW and 1 s (curves 2 and 4). (e) A Raman spectra of the original dry placental  $\text{dsDNA}_{\text{pl}}$  deposited on pure Si support; the spectrum was recorded at laser excitation wavelengths of 473 nm; the laser power and collected time were used for the specimen excitation: 5.76 mW and 60 s. “\*” denotes a laser mode.

one gets the index  $(n, m) = (7, 4)$  for the SWCNTs. It is a sign of the fact that they are of metal type because  $\text{mod}[(n - m), 3] = 0$ .

So-called D and G graphene Raman bands in the Raman spectra for the broken-down (crumpled) LB-monolayer formed by the micellar  $\text{KRAS}_w$ -FWCNTs hybrids and the micellar  $\text{DNA}_{\text{pl}}$ -CNT hybrids are very intensive (see Fig. 1). The D peak is defect-activated one because it is highly intensive if the graphene structure is disturbed. The G peak is an in-plane vibrational mode that involves  $\text{sp}^2$  hybridized carbon atoms that comprises the graphene sheet. To find DNA one utilizes a DNA intercalating dye, for example, propidium iodide (PI). PI fluorescence grows when

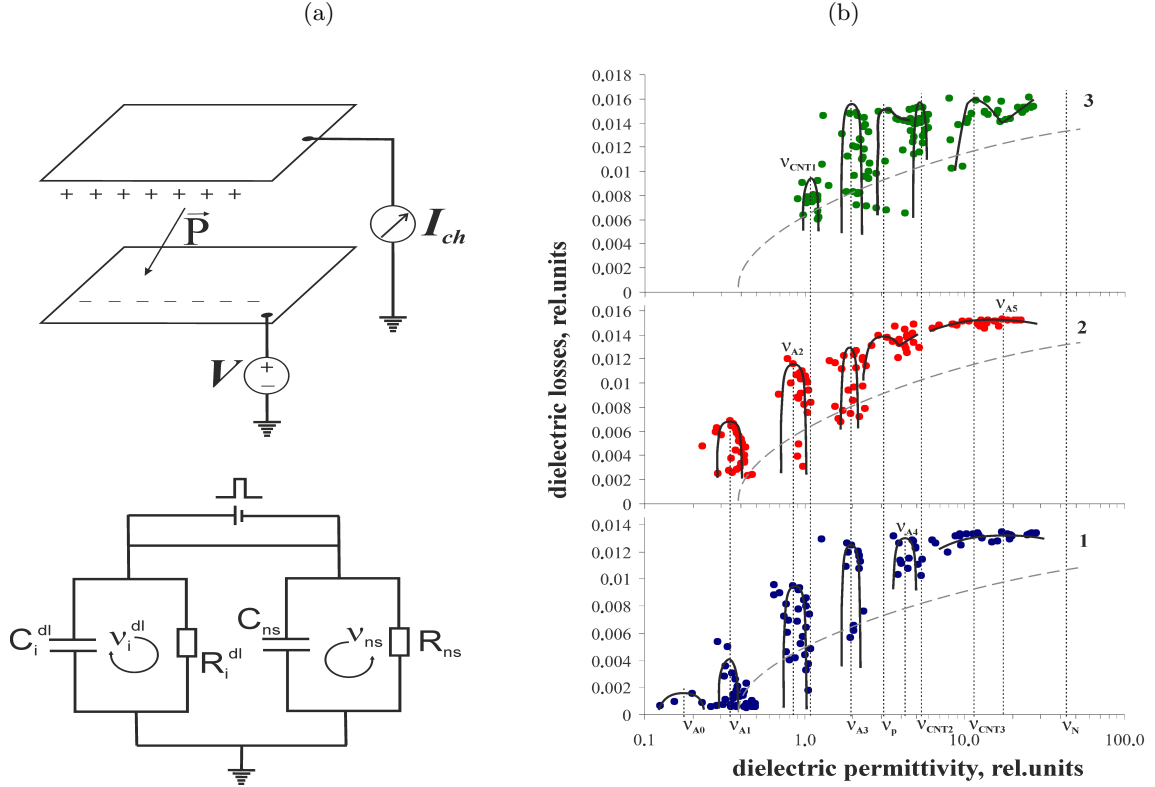


FIG. 3: (a) Cartoon of the scheme of the sensor operation based on a dielectric-polarization relaxation process (up) and an equivalent circuit diagram of the sensor (down). A square voltage pulse with a bias is applied to the sensor to excite the autooscillations;  $\vec{P}$  is the polarization vector. (b) Dielectric spectra “1” for nanoporous AOA, “2”, and “3” for nanoheterostructure based on the nanocyclic compound Fe(II)DTP and on the decorated FWCNTs, respectively. Quasiresonance frequencies of Cole-Cole plots in the spectra are marked as  $\nu_{Ai}$ ;  $i = 0, \dots, 5$  for AOA;  $\nu_P$  for the organometallic compound and  $\nu_{CNTi}$ ,  $i = 1, 2, 3$  for FWCNTs. A Nyquist plot of impedance for the measuring circuit is marked by a yellow dashed line with  $\nu_N$ . The dielectric losses and permittivity were measured in inverse-capacity units of  $\text{pF}^{-1}$  and in power units of  $\text{V}^2$ .

the PI molecules intercalate into the DNA molecule. It is used to indicate the presence of DNA. As Fig. 1c shows, such PI fluorescence is observed for the samples under investigation.

The crystal structure of the KRASw-FWCNT LB-monolayer or high-ordered self-organized micellar structure change during crumpling of the LB-monolayer or due to misfolding of the CNTs in the inverse micelles. The high intensity of the D peaks of the Raman spectra shown in Fig. 1 steams from the fact that there are isolated structural defects in the DNA-CNT hybrids. However, since the metallic single walled CNTs are flexible they can be arranged with a high degree of order. In this case, the D and G peaks can be very weak in the Raman spectra of DNA-CNT hybrids (see Figs. 2(a, red curve) and (d, red and green curves 3 and 4)). Prominent peaks in these Raman spectra in the Figs. 2(a, red curve) and (d, red and green curves 3 and 4) indicate the DNA molecular group vibrations because their frequencies coincide with all characteristic bands of micellar dsDNAs in recorded Raman DNA spectra presented in Figs. 2(a, blue curve), (b)–(d) [26].

Comparing the DNA Raman spectra shown in Fig. 2a before and after their complexification with the high-ordered arrays of the metallic CNTs one concludes that the intensity of the DNA Raman bands is increased. This occurs in a result of the complexification with the metallic CNTs and, correspondingly, the CNTs can enhance the light scattering in the DNA layers. It signifies that there are graphene patches which host Klein resonances provided that the bulk graphene is doped. The Klein resonance is excited by an electric field (for example, the electric field of an electromagnetic pulse). Such areas are called electrostatically-confined graphene  $p-n$  ( $n-p$ ) junctions [19]. The confinement is explained by the occurrence of Klein resonances as a result of Klein oblique tunneling of the massless graphene charge carriers (holes or electrons) through these graphene patches. It was proved in [20] that the Klein resonances have a topologically non-trivial origin. They exist due to non-Abelian statistics of the graphene fermions, but not due to the chirality of pseudo Dirac fermions. The obliquity of the Klein-tunneling graphene charge carriers moving in the CNT samples emerges as a result of the electrical dipole moment action from the side of the DNA molecular groups.

The topologically-nontrivial graphene charge carriers are vortex and antivortex Majorana excitations (modes) or their cores in the graphene electron density [13–16, 18]. The Klein resonances and, correspondingly, the pairs of Majorana modes are arranged on a crystal lattice if the DNA-CNT hybrids form a superlattice structure. A number of the Majorana modes is giant owing to the fact that a topological-charge conservation law impedes their annihilation. When the free pseupo-Majorana modes oscillate at the eigenfrequencies of molecular DNA groups, plasmon resonances arise. Their intensities are much higher than ones of the proper DNA vibrations because the huge number of the Majorana modes. It explains the CNT-enhanced scattering of light in the DNAs which Raman spectra are presented in Fig. 2a.

The low intensity of the DNA Raman peaks in the broken (crumpled) LB-monolayer is due to the fact that the isolated hybrid structural defects play the role of disorderly-arranged impurities residing in the Klein-resonance superlattice. To satisfy a Pauli exclusion principle, the graphene pseudo-Majorana fermion pairs occupy higher electronic impurity levels and, correspondingly, prevent electrons of the aromatic molecular groups from passing to these high-energy levels. This phenomena is called a fluorescence quenching in the graphene plane. In this case the number of negative (positive) charge carriers prevails over the number of positive (negative) charge carriers in graphene. As a result, the Dirac  $K(K')$  point of the graphene Brillouin zone turns out to be electrically charged. Oscillations of C nuclei near the charged Dirac  $K(K')$  point originate the D Raman peak because the charged  $K(K')$  point plays the role of an electronic term. If the Raman peak intensity is high enough, for example, as in the Raman spectra shown in Fig. 1, then weakly intensive vibrations of the DNA molecular groups are barely visible on its background.

DNA Raman spectra are strongly affected by deprotonation. Due to the latter Raman spectral bands of DNA are widened even for a dry DNA sample (see the Raman spectrum of the dry dsDNA<sub>pl</sub> deposited on pure Si support in Fig. 2e). Hampering the deprotonation the stearic-acid shell of the inverse micelles drastically narrows Raman spectral bands in the Raman spectra for the micellar dsDNA and dsDNA–CNT-hybrid deposited on pure Si (make comparison between the Raman spectra presented in Figs. 2a,b, and e).

Raman spectra for the micellar dsDNA<sub>pl</sub> dropped on a Si surface hydrophilized by the H-DTP molecules are significantly widened in comparison with the spectra of the micellar DNAs deposited on the non-modified Si surface (compare the two Raman spectra “1” and “2” shown in Fig. 2d with the Raman spectra in Figs. 2(a, blue curve) and (b)). However, the complexification of the dsDNA<sub>pl</sub> with the carbon nanotubes leads to the confinement of the placental DNA on the hydrophobic CNT surface by the  $\pi - \pi$  stacking interactions and, correspondingly, to a DNA protonation. The narrowing of the Raman spectrum of the micellar DNA<sub>pl</sub>-CNT hybrids testifies the DNA protonation (make comparisons between the values of spectral widths in the Raman spectra “1”–“4” shown in Fig. 2d).

## B. Principle of operation of capacitive transducer

Electrophysical properties of the ultra-thin LB-films were studied by means of the impedance spectroscopy methods as a variation in dielectric polarization of a near-electrode Helmholtz double electrically charged layer formed at the interface between a surface of the fabricated electrochemical sensor and water. The non-faradaic impedimetric sensor operates on surface-polarization-decreasing effects which are originated by the conducting ultra-thin LB-films when shielding the near-electrode Helmholtz layer. A scheme of the sensor operation is presented in Fig. 3(a). As Fig. 3(a, up) shows, the discharging (charging) current  $I_{ch}$  produces the bias  $V$  in the RC oscillator. A polarization  $P$  of near-electrode layers is proportional to the applied bias  $V$ :  $\Pi P \propto V$ , where  $\Pi$  is a polarizability. On the other hand,  $P$  is the induced charge density  $\delta n$  due to the charging (discharging) of the capacitor so that the charging (discharging) current  $I_{ch}$  is proportional to  $\delta n$ :  $P \sim \delta n \sim I_{ch}$ . Since  $P$  is determined through a complex dielectric permittivity  $\epsilon$  by the following formula:  $\epsilon = 1 - \Pi$ , one gets that

$$I_{ch} \propto \frac{V}{1 - \epsilon}. \quad (\text{III.3})$$

The dielectric losses  $\epsilon''$  due to the dielectric-polarization relaxation process occur in a frequency range where the sensor capacitance  $C$  falls down. The  $\epsilon''$  is the imaginary part of the complex dielectric permittivity:  $\epsilon = \epsilon' + i\epsilon''$ , and, correspondingly, presents a resistivity because [37]

$$\epsilon = 1 + i \frac{\sigma}{\epsilon_0 \omega}. \quad (\text{III.4})$$

Here  $\sigma$  is the conductivity,  $\epsilon'$  is the dielectric permittivity,  $\omega$  is the cyclic frequency,  $\epsilon_0$  is the electric constant. It follows from the last equation and Eq. III.3 that

$$I_{ch} \sim \Im m \frac{V}{1 - \epsilon} \sim \Re e \frac{\epsilon_0 \omega V}{\sigma} \sim \frac{V}{\epsilon''}. \quad (\text{III.5})$$



But, an energy  $CV^2/2$  stored at (released from) the capacitance  $C$  is determined by the following expression:  $CV^2/2 \sim I_{ch}V$ . Substituting the expression (III.5) for the  $I_{ch}$  into the expression for the energy one can assume that  $\epsilon'' \sim 1/C$ . The signal power  $W$  recorded by the Fourier analyzer is proportional to the real part of the complex dielectric permittivity  $\epsilon'$  because  $W$  is the stored energy determined by the following equation:  $W \sim |\vec{D} \times \vec{H}|$  with the electric displacement vector  $\vec{D} = \epsilon' \vec{E}$ , where  $\vec{E}$  and  $\vec{H}$  are electric and magnetic fields vectors, respectively.

Let us suppose that  $N$  dipole-polarization processes proceed inside the Helmholtz layer emerging near the  $N$  electrode pairs. It signifies that an equivalent circuit diagram of both the capacitor-charging (capacitor-discharging) and polarization processes consists of  $(N+1)$  RC circuits. The equivalent circuit of the sensor presents in Fig. 3(a, down). As one can see forced oscillations with a frequency  $\nu_i$  can be generated in the  $i$ -th parallel  $R_i^{dl}C_i^{dl}$  circuit for which the double-layer resistance  $R_i^{dl} \equiv R_i$ ,  $i = 1, \dots, N$  is much more than the instrument resistance  $R_{ns}$  in some frequency range  $\nu_i \pm \Delta_i$ . If  $R_i \ll R_{ns}$  then the forced oscillations with a frequency  $\nu_{ns}$  are generated in the properly measuring  $R_{ns}C_{ns}$  circuit. Thus, the dependence of  $1/C$  on  $W$  will present  $N$  Cole-Cole plots and one Nyquist impedance plot for parallel connection of the capacitor to the instrument resistor  $R_{ns}$  (see Fig. 3b). Since  $R_i \gg R_{ns}$  the capacitance  $C$  of the sensor can be calculated by the formula  $C = 1/(2\pi R_{ns}f)$ .

The charge density of the graphene monolayers deposited on the interdigital electrode structure in deionized water can be indirectly resonantly swung by the low-frequency resonant decay of the hydrated ion complexes, which are in an excited state, and subsequent association of the ions  $\text{OH}^-$  and  $\text{H}^+$  into water molecules. Meanwhile, emitting electromagnetic quanta the water molecules pass to a low-lying state. The electromagnetic field excites the graphene-charge-density oscillations. Resonating with dipole moments of the hydrated complexes of the near electrode double charged layer, the graphene plasmon oscillations decay the hydrated complexes in the Helmholtz double layer and, correspondingly, screen effectively the electrodes [38].

Dielectric spectra of the AOA isolating layer, Fe(II)DTP LB-film, and FWCNT LB-arrays under investigation are shown in Fig. 3b. The dielectric spectra of AOA do not have specific dielectric Cole-Cole plots with a Warburg diffusion element or Warburg impedance,  $Z_W$ . Since the Warburg impedance is absent for AOA and, consequently, aluminium-electrodes oxidation does not happen, the fabricated nanoheterostructures are stable.

The  $Z_W$  impedance element is created by the diffusion layer in which the electrochemical reactions with a mass transfer proceed due to electrochemical reactions. The impedance measurements for the metal-containing dithiynylpyrrole LB-films entering the Helmholtz double layer indicate the depressed semi-circle with the Warburg diffusion tail in the Cole-Cole plot of the dielectric spectrum “2” shown in Fig. 3b. For the dithienylpyrrole LB-films, this oxidation-reduction potential (potential stipulated by a change of molecular-group charge state) arises due to self-redox activity of pyrrole residue leading to the transport of electrical charge along the chain of conjugated double bonds. The FWCNT LB-arrays are redox active themselves also because a Warburg impedance element is visible in the corresponding Cole-Cole plot of the dielectric spectrum “3” shown in Fig. 3b. The change of charge state of valleys  $K(K')$  (Dirac points) of the graphene Brillouin zone in the momentum space is associated with the mass transfer that Kitaev-like chains with Majorana end states emerge. Meanwhile, plasma oscillations of produced electron-hole pairs shield electric field of charged electrodes.

In [39] a method to detect the DNA hybridization leading to a homoduplex formation at low temperatures has been proposed. This method operates on the enhancement of the electric-field FWCNT screening when the FWCNTs are linked to each other by dsDNA and as a result a high-conductivity network is created.

### C. Dielectric spectral analysis of low-temperature DNA hybridization

Now, let us study a toehold exchange reaction between the dsDNA “P3/W3” and the ssDNA “N3” proceeds in the DNA chip. The formation of the P3/N3 homoduplex in the result of the toehold exchange reaction between the dsDNA “P3/W3” and the ssDNA “N3” is detected as an rise of the dielectric losses,  $1/C$ . When hybridizing the toehold DNA probes the N3 ssDNA target in the temperature range from RT to 34 °C because the dielectric-loss spectral peak grows in this temperature range due to increasing the electrode shielding degree by the sensing covering after the homoduplex formation as Fig. 4 shows.

The Bode peak intensities vary weakly for the temperatures of 30, 32, 34, 36, 38, 40, 50 °C and largely enough for 60, 65, 70 °C in comparison with the intensity of the peak at RT (see Fig. 4). One observes an abrupt change (drop) of the dielectric losses at 60 °C. The drastic drop of the spectral peak intensity at 60 °C indicates that defects appear in the sensitive coating due to a disruption of the stacking  $\pi-\pi$  interaction and of the hydrogen bonds between complementary nucleotide pairs in the DNA homoduplexes. This screening-effect attenuation testifies that dsDNA melting occurs.

A similar stepwise drop of the dielectric losses, but on a smaller scale, is observed at 50 °C because the intensity of the Bode plot peak at 50 °C drops significantly more than the intensities of the nearby Bode plots for the following

temperatures: 36, 38, and 40 °C.

Such universal scaling dielectric losses behavior allows us suggest that the systems undergoes a first-order phase transition. Thus the existence of the temperature scaling indicates that the process of dsDNA dissociation on the surface proceeds similarly to a phase transition of the first order.

The DNA-melting temperature  $T_m$  is indicated as the temperature at which the effect of the electrode-electric-field screening disappear. The dielectric losses increase with the increase in temperature up to the temperature of 34 °C. Then, with the increase in temperature to the temperature of 36 °C the intensity of the dielectric losses are reduced. It means that a value of  $T_m$  is close to 36 °C.

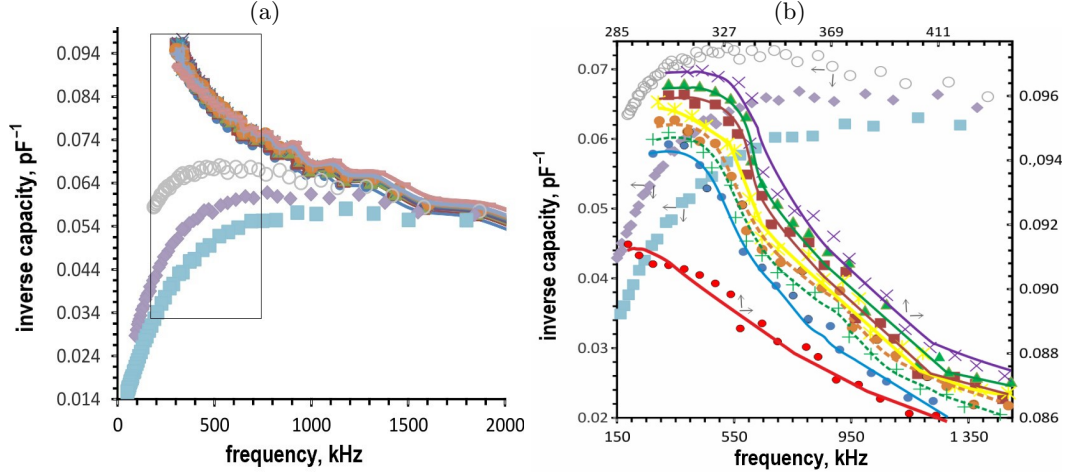


FIG. 4: Bode plots at different temperatures for P3/N3 homoduplexes. Brown, green, yellow, red and blue solid curves fit the data labeled by symbols of corresponding color: brown squares “■” for 30 °C, green triangles “▲” for 32 °C, violet “×” for 34 °C, yellow “\*” for 36 °C, red circles “●” for 50 °C, blue circles “●” for RT. Light brown, green dashed curves fit the data labeled by symbols of same color: light brown circles “●” for 38 °C, green “+” for 40 °C. The data labeled by open gray circles “○”, light violet rhombuses “◇”, and light blue squares “□” present dielectric loss at 60, 65, and 70 °C, respectively. Inset (b): the designed fragment of the figure (a) is shown on a large scale.

#### Sensitivity of label-free electrochemical impedimetric DNA-chip.

As one can see in Fig. 5, the binding of the DNA probe with hydrophobic sensor surface occurs as the capacity decrease is observed. This screening effect is provided by  $\pi$ - $\pi$  interaction between the DNA probe nucleotide sequence and the surface of the carbon nanotubes. The capacity decrease is of, for example, 2 pF at 150 kHz. Accordingly to the experimental data presented in Fig. 5, the replacement of the “weak” inosine-contained chain “W3” entering the toehold probe “P3/W3” by the perfect-matched target ssDNA “N3” occurs at room temperature. The screening effect as a result of the complementary hybridization holds in the all frequency range. The sensor electrodes are shielded both at picomolar and attomolar concentrations of the DNA target.

When adding the single-mismatched target ssDNA “M3” increases the sensor capacity  $C$  significantly that is stipulated by the bulk charge density increase. The large bulk charge density appears because the non-specific links between the non-complementary target and probe DNA molecules and, as a result, gapping between the DNA probe and target that leads to dipole polarization and ionization of the sugar phosphate backbone.

After washing of the P3/M3 heteroduplexes, the capacity of the sensor returns to its pre-hybridization value. It signifies that the heteroduplexes do not penetrate into the nanopores and are held on the sensor surface by electrostatic forces if there is no first-order phase transition. Correspondingly, the heteroduplexes are easily washed away because of the weakness of the electrostatic forces.

So, a network is created by linking together FWCNTs through dsDNA homoduplexes that results in the increase of sensor-shielding degree.

## IV. KRAS-GENE SEQUENCING

### A. Micellar genotyping based on quenching effect

Forming a high-conducting network of CNTs linked by DNA molecules the complexification of highly-ordered CNT arrays with DNA does not impair but vice versa improves the ability of the CNT arrays to screen electromagnetic

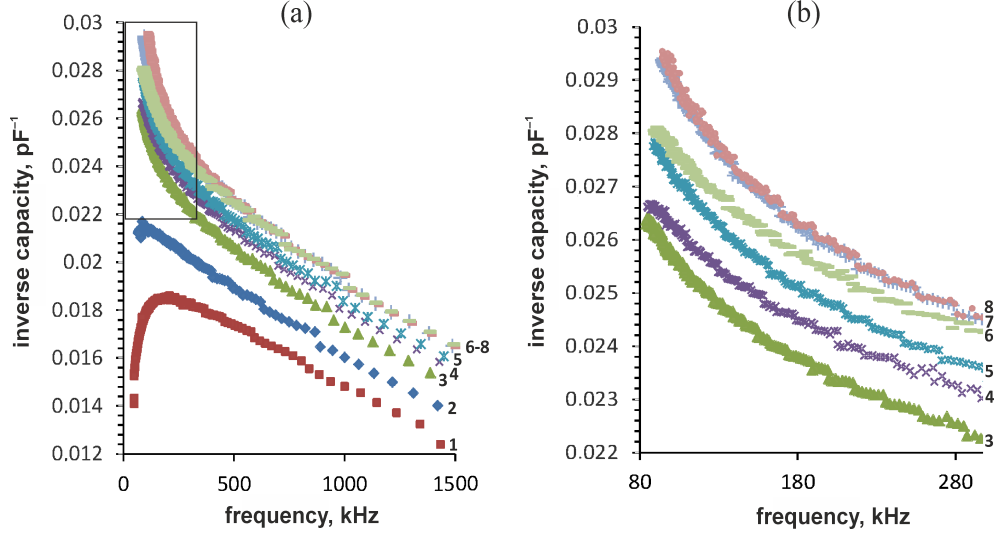


FIG. 5: Bode plots at different concentration of the target DNA after hybridization between the N3 or M3 ssDNA target and toehold probe P3/W3 : the plot “1” (brown squares “■”) for the pure sensor; the plot “2” (blue rhombus “◆”) for the DTP sensor coating; the plot “3” (green triangles “▲”) for the polyG-FWCNT hybrids; the plot “4” (violet criss-crosses “×”) for the P3/W3 probe; the plots “5”–“7” for the P3/N3 homoduplexes forming at the target concentration of  $10^{-18}$ ,  $10^{-14}$ , and  $10^{-12}$  mol/ $\mu$ L, respectively; the plot “8” for the mutant M3 ssDNA target hybridized with the P3/W3 toehold at the M3 concentration of  $10^{-18}$  mol/ $\mu$ L. Inset (b): the designed fragment of the figure (a) is shown on a large scale. The hybridization proceed at RT.

fields. Meanwhile, the ssDNA–CNT hybrids have to be disordered enough so that when occupying the impurity energy levels the graphene pseudo-Majorana charge carriers would quench the light scattering in DNA.

A perfect network of DNA–CNT hybrids is formed by links between the  $\text{KRAS}_m$ -dsDNA<sub>C6</sub>-CNT hybrids but not by links between the  $\text{KRAS}_w$ -dsDNA<sub>C6</sub>-CNT hybrids because the intensity of the Raman D-peak is significantly less for the  $\text{KRAS}_m$ -dsDNA<sub>C6</sub> duplexes (compare Raman spectra in light- and dark-blue lines in Fig. 6a). The attenuation of the quenching effect indicates that the  $\text{KRAS}_m$ -dsDNA<sub>C6</sub>-CNT network is more perfect and when hybridizing the  $\text{KRAS}_m$  primers and dsDNA<sub>C6</sub> molecules form homoduplexes. Moreover, the intensity of the  $\text{KRAS}_w$ -dsDNA<sub>C6</sub>-heteroduplex Raman bands (see the frequency region from 2700 to 3100  $\text{cm}^{-1}$  in the Raman spectra in light-blue lines in Fig. 6a) is significantly higher than one of the  $\text{KRAS}_m$ -dsDNA<sub>C6</sub>-homoduplex Raman bands (see the frequency region from 2700 to 3100  $\text{cm}^{-1}$  in the Raman spectra in dark-blue lines in Fig. 6a). It testifies that DNA interior of the micelles hosting  $\text{KRAS}_m$ -dsDNA<sub>C6</sub> duplexes is shaded from the laser radiation by the  $\text{KRAS}_m$ -dsDNA<sub>C6</sub>-CNT network better than the  $\text{KRAS}_w$ -dsDNA<sub>C6</sub>-CNT network due to the fact that surface of the  $\text{KRAS}_m$ -dsDNA<sub>C6</sub>-CNT micelles is covered by the highly screening network created in the result of the complementary hybridization.

Thus, creating the network the homoduplexes link the FWCNT together so that the degree of ordering of the micellar DNA-CNT hybrids increases after hybridization.

## B. Micellar genotyping on plasmon-resonance effect

The micellar genotyping on the plasmon-resonance effect is performed in a following way. One detects a light scattering enhancement in duplexes between the target and probe DNAs and subsequently a dependence of this enhancement on the DNA–CNT hybrid type is analyzed.

The plasmon resonance as well as the screening effect occurs at high enough density of the charge carriers in the graphene valleys  $K, K'$ . As the non-specific linked target DNA is kept on a long enough distance from the micelles surface, the light scattering in the non-complementary hybridized target DNA is not quenched because no transitions of the graphene charge carriers to non-occupied impurity energy levels occur. The higher intensity of the DNA Raman bands for the  $\text{KRAS}_w$  probe–target DNA duplexes hybridized with FWCNTs in comparison with the intensity of the Raman spectrum of the micelles with the original DNA testifies the FWCNT-enhanced light scattering for the DNA (compare black and green curves in Fig. 6a). To produce the plasmon oscillation DNA molecules should reside outside the micelles surface so that the DNA-molecular groups vibrate out of graphene plane and, accordingly, are not quenched.

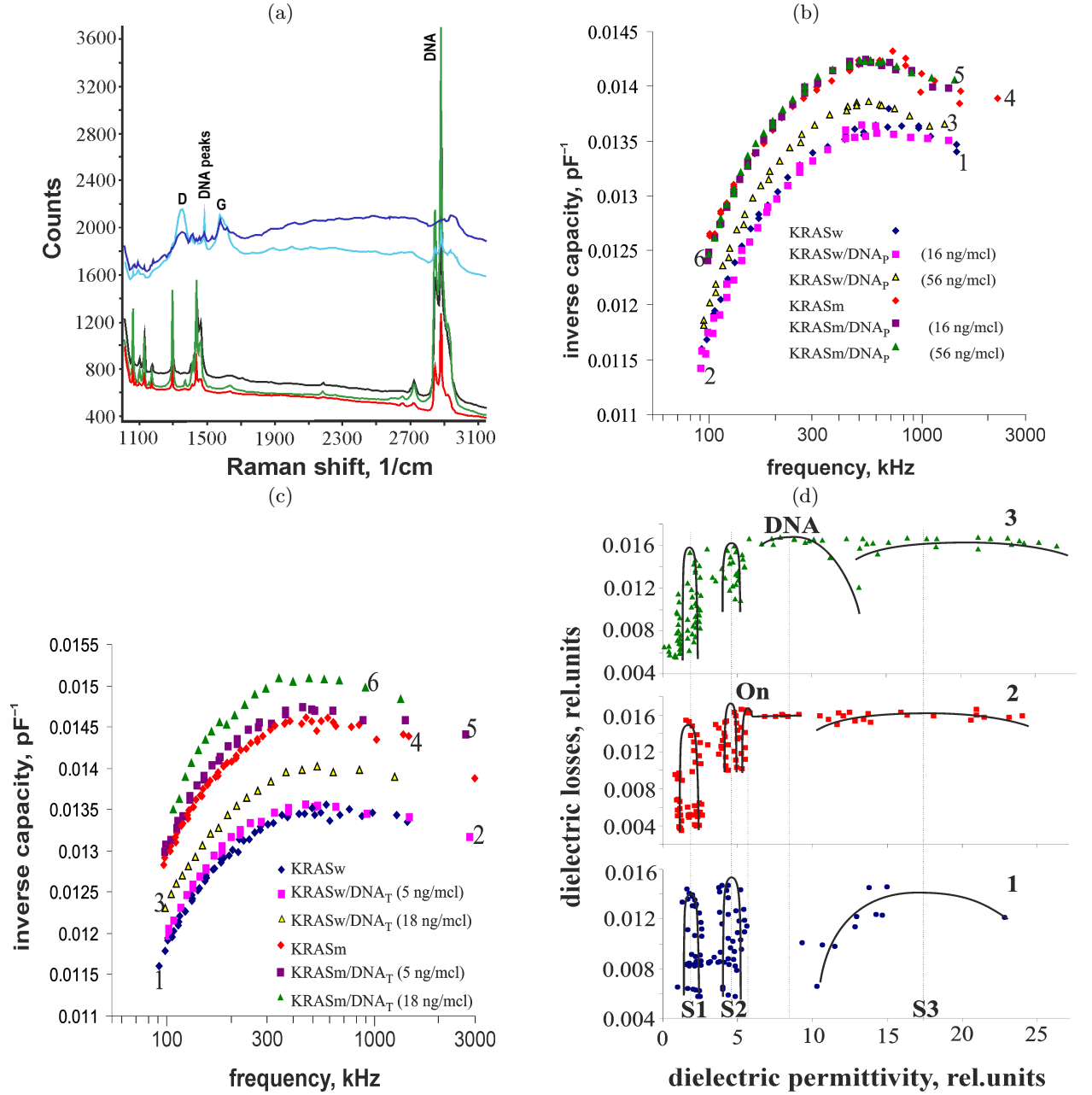


FIG. 6: Raman spectral (a) and EIS (b-d) genotypings. (a) Raman spectra of inverse micelles with DNA<sub>C6</sub> isolated from C6-line cells (black curve), of imperfect micellar FWCNTs covered by DNA molecules hybridized with KRAS<sub>w</sub>- or KRAS<sub>m</sub>-oligonucleotides (light- and dark blue curves, respectively), and of high-ordered micellar FWCNTs covered by DNA molecules hybridized with KRAS<sub>w</sub>- or KRAS<sub>m</sub>-oligonucleotides (green and red curves, respectively). The spectra were recorded at laser excitation wavelengths of 532 nm; the laser power and collected time were used for the specimen excitation: 2 mW and 60 s, respectively. (b-c) Bode plots for sensors before (1, 4) and after (2,3,5,6) hybridization between perfectly matched and single-nucleotide mismatched ssDNA probe with native DNA<sub>pl</sub> (b) and DNA<sub>CRC</sub> (c). DNA concentrations used are indicated in brackets. (d) Dielectric spectra: “1” and “2” for the DNA-sensor with KRAS<sub>w</sub> probe and KRAS<sub>w</sub>-ssDNA<sub>tp</sub>/ssDNA<sub>wm</sub> toehold probe system, respectively; “3” after binding with the target ssDNA<sub>tm</sub>. Cole-Cole plots are labeled by  $S_i$ ,  $i = 1, 2, 3$  for the DNA-sensor with KRAS<sub>w</sub> only; “On” for the dsDNA toehold probe, and “DNA” for the homoduplexes, respectively. The dielectric losses and permittivity were measured in inverse-capacity units of  $\text{pF}^{-1}$  and in power units of  $\text{V}^2/\text{V}$ .

The intensity of the micellar DNA<sub>C6</sub>-FWCNT-hybrid Raman bands for the homoduplexes, dsDNA<sub>C6</sub>-KRAS<sub>m</sub>, of the target dsDNA<sub>C6</sub> with the mutant-type probe, KRAS<sub>m</sub>, are less than for the heteroduplexes, dsDNA<sub>C6</sub>-KRAS<sub>w</sub>, of the target dsDNA<sub>C6</sub> with the single-base mismatched oligonucleotide (as one can see from comparison between the Raman spectra in red and green lines in Fig. 6a). It signifies that a perfect high-conducting network of the homoduplex-CNT hybrids is produced and when arranging on the micelles surface a patch of the network is shaded KRAS<sub>m</sub>-dsDNA<sub>CRC</sub>-CNT hybrids residing in the inside of the micelles from the laser radiation.

### C. Electrochemical genotyping based on screening effects of crystalline CNT LB-arrays

We present a micellar genotyping electrochemical technology to discriminate a single nucleotide mutation in the KRAS gene (2 exon, 12 codon, G/A). To recognize the mutant and wild alleles, it was necessary to use two sensors. The wild-type allele detection probe was placed on the surface of the first sensor. The probe for detection of the mutant type allele was located on the surface of the second sensor.

This technology is based on the screening effect leading to that the capacity values for a wide frequency range decrease as a result of the complementary hybridization between the target and the probe DNA sequences. The degree of sensor electrodes shielding increases after complementary hybridization between the wild-type dsDNA<sub>p1</sub> and KRAS<sub>w</sub> probe. At that time the capacity of sensor decreases accordingly to its Bode plots for different dsDNA<sub>p1</sub> concentrations (see Fig. 6b). No binding between the dsDNA<sub>p1</sub> target and KRAS<sub>m</sub> probe occurs. The transducer do not response on the KRAS mutation as Fig. 6b shows. The shielding effect is observed for the dsDNA<sub>CRC</sub> target hybridized both with KRAS<sub>m</sub> and KRAS<sub>w</sub> probes. The capacity decreases in both cases (see Fig. 6c). It signifies that both wild- and mutant-type of KRAS-oncogene were detected.

Thus, the sequencing method has allowed us to diagnose allele SNP of the KRAS-oncogene in the genome of the colorectal cancer tissue. It testifies allele SNP of KRAS-oncogene in the genome of the colorectal cancer tissue.

To study the selectivity of the DNA nanosensor a DNA chip has been designed. Two probes, the KRAS<sub>w</sub>-CNT LB-hybrids and the 47-base oligonucleotide toehold probes of mutant type presented in Table I, have been located on the chip surface. A mass transfer for the 47-base toehold probe-FWCNT hybrids is observed, as the dielectric spectrum of the EIS-transducer including the dsDNA toehold probe-FWCNT hybrids is characterized by the presence of a Warburg impedance in the Cole-Cole plot labeled by "On" for the dielectric spectrum "2" shown in Fig. 6d. It testifies redox activity of the dsDNA probe on the FWCNT surface. Fig. 6(d) shows also that a Cole-Cole plot of homoduplex (Cole-Cole plot labeled by "DNA" in the dielectric spectrum "3") appears after specific complementary hybridization. Any signs of transducer response on the heteroduplex formation are not observed.

Thus, DNA molecules being non-specific bonded with DNA probes are easily washed and do not contribute in the transducer response.

## V. DISCUSSION AND CONCLUSION

So, the experimental studies performed have revealed that no hybrid formation can occur due to the stacking interactions between  $\pi(p_z)$  electrons of carbon nanotubes and DNA molecules only. The observed CNT-enhanced scattering of light in dsDNA and shielding effects of DNA hybridization are explained by the topologically non-trivial Majorana nature of the graphene charge carriers. the graphene topologically non-trivial charge carriers they transit to DNA non-occupied energy levels. The stacking  $\pi - \pi$  interaction can be originated by the Klein resonances which are created by Klein-tunneling graphene topologically non-trivial charge carriers and subsequently transit to DNA non-occupied energy levels.

The conservation law of topological charge forbids annihilation between the pseudo-Majorana graphene charge carriers and the DNA charge carriers. It signifies that a lifetime of the pseudo-Majorana particles on the overlying impurity DNA levels is long. The graphene charge carriers excited to the impurity energy levels do not annihilate with electrons or holes of the impurity because their statistics is non-Abelian. The disappearance (quenching) of the light scattering stems from the non-Abelian statistics owing to impossibility to excite DNA electrons on the overlying levels due to the Pauli exclusion principle.

Sharp decrease of the intensity of the CNT Raman bands up to it fully disappearing occurs in strong electrical fields of superlattices formed by the DNA-CNT hybrids. Meanwhile, the scattering of light in the aromatic molecular DNA groups residing away from the graphene plane is enhanced because the light is scattered on intensive graphene-charge-density oscillations emerging in resonance with low-intensity vibrations of the aromatic molecular groups. The conducting properties of the DNA transducer are improved at the complementary hybridization. The screening of the light scattering by the homoduplex-CNT hybrids is so amazingly effective that the incident electromagnetic quanta do not reach and, accordingly, do not excite the DNA vibration with subsequent generation of the CNT plasma

oscillations at eigenfrequencies of DNA vibrations.

The DNA–CNT hybrid high-ordered coverings effectively shield near-electrode double charged layers. The new high-performance DNA nanosensor which operation is based on a difference in efficiency of the shielding by the ssDNA–CNT hybrid networks before hybridization and dsDNA–CNT networks forming after complementary hybridization have been developed to genotype DNA sequences from fragmented FFPE nucleic acid samples with limit detection up to attomolar concentrations.

Finalizing, dielectric and Raman spectral studies of DNA hybridization on surface of metallic single-walled carbon nanotubes decorated by organometallic compound and suspended on nanopores have been performed. It has been shown that self-redox activity of the carboxylated CNTs decorated by the nanocyclic organometallic complexes can be used to discriminate single-nucleotide polymorphism of colorectal tumor genome.

We offer the two DNA-sequencing methods based on shielding effects or enhancement of light scattering by DNA–single-walled metallic carbon nanotube hybrids. Both the high-performance genotyping assays operate at room temperature. The impedimetric DNA sensors of non-faradaic type based on the screening effect can be more sensitive than the Raman optical transducer based on the quenching effect due to liability of the Raman transducer parameters to environmental influence. Our high performance DNA sensor will be at an advantage over the plasmon-resonance sequencer when performing single-molecule allele discrimination of the genome of metastatic tumor cells at early and first stages of cancer.

- 
- [1] FDA Approves First KRAS Inhibitor: Sotorasib. *Cancer Discov.* 2021 Aug;11(8):OF4. doi: 10.1158/2159-8290.CD-NB2021-0362.
  - [2] Nakajima EC, Drezner N, Li X, Mishra-Kalyani PS, Liu Y, Zhao H, Bi Y, Liu J, Rahman A, Wearne E, Ojofeimi I, Hotaki LT, Spillman D, Pazdur R, Beaver JA, Singh H. FDA Approval Summary: Sotorasib for KRAS G12C-Mutated Metastatic NSCLC. *Clin Cancer Res.* 2022 Apr 14;28(8):1482-1486. doi: 10.1158/1078-0432.CCR-21-3074.
  - [3] Arora S, Balasubramaniam S, Zhang H, Berman T, Narayan P, Suzman D, Bloomquist E, Tang S, Gong Y, Sridhara R, Turcu FR, Chatterjee D, Saritas-Yildirim B, Ghosh S, Philip R, Pathak A, Gao JJ, Amiri-Kordestani L, Pazdur R, Beaver JA. FDA Approval Summary: Olaparib Monotherapy or in Combination with Bevacizumab for the Maintenance Treatment of Patients with Advanced Ovarian Cancer. *Oncologist.* 2021 Jan;26(1):e164-e172. doi: 10.1002/onco.13551.
  - [4] Panchal NK, Bhale A, Chowdary R, Verma VK, Beevi SS. PCR Amplifiable DNA from Breast Disease FFPE Section for Mutational Analysis. *J Biomol Tech.* 2020 Apr;31(1):1-6. doi: 10.7171/jbt.20-3101-001.
  - [5] Kapp JR, Diss T, Spicer J, Gandy M, Schrijver I, Jennings LJ, Li MM, Tsongalis GJ, de Castro DG, Bridge JA, Wallace A, Deignan JL, Hing S, Butler R, Verghese E, Latham GJ, Hamoudi RA. Variation in pre-PCR processing of FFPE samples leads to discrepancies in BRAF and EGFR mutation detection: a diagnostic RING trial. *J Clin Pathol.* 2015 Feb;68(2):111-8. doi: 10.1136/jclinpath-2014-202644.
  - [6] Lu XJD, Liu KYP, Zhu YS, Cui C, Poh CF. Using ddPCR to assess the DNA yield of FFPE samples. *Biomol Detect Quantif.* 2018 Nov 7;16:5-11. doi: 10.1016/j.bdq.2018.10.001.
  - [7] Li CC, Hu J, Luo X, Hu J, Zhang CY. Development of a Single Quantum Dot-Mediated FRET Nanosensor for Sensitive Detection of Single-Nucleotide Polymorphism in Cancer Cells. *Anal Chem.* 2021 Nov 2;93(43):14568-14576. doi: 10.1021/acs.analchem.1c03675.
  - [8] Tadmety A, Zhang Y, Molinski JH, Palinski TJ, Tsongalis GJ, Zhang JXJ. Plasmonic Nanoparticle Conjugation for Nucleic Acid Biosensing. *Methods Mol Biol.* 2022;2393:73-87.
  - [9] Nesvet JC, Antilla KA, Pancirer DS, Lozano AX, Preiss JS, Ma W, Fu A, Park SM, Gambhir SS, Fan AC, Neal JW, Padda SK, Das M, Li T, Wakelee HA, Wang SX. Giant Magnetoresistive Nanosensor Analysis of Circulating Tumor DNA Epidermal Growth Factor Receptor Mutations for Diagnosis and Therapy Response Monitoring. *Clin Chem.* 2021 Mar 1;67(3):534-542. doi: 10.1093/clinchem/hvaa307.
  - [10] Kim N, Kim E, Kim H, Thomas MR, Najer A, Stevens MM. Tumor-Targeting Cholesterol-Decorated DNA Nanoflowers for Intracellular Ratiometric Aptasensing. *Adv Mater.* 2021 Mar;33(11):e2007738. doi: 10.1002/adma.202007738.
  - [11] J. Li, Zh. Chen, Yu Xiang, L. Zhou, T. Wang, Zh. Zhang, K. Sun, D. Yin, Yi Li and G. Xie, “An electrochemical biosensor for double-stranded Wnt7B gene detection based on enzymatic isothermal amplification,” *Biosensors and Bioelectronics*, vol. 86, pp. 75-82, 2016.
  - [12] J. Quinchia, D. Echeverri, A.F. Cruz-Pacheco, M.E. Maldonado, and J. Orozco. Electrochemical biosensors for determination of colorectal tumor biomarkers. *Micromachines.* **11**, paper 411 (2020).
  - [13] H. Grushevskaya, G. Krylov. Polarization in quasirelativistic graphene model with topologically non-trivial charge carriers. *Quantum Rep.* **4**, 1-15 (2022). <https://doi.org/10.3390/quantum4010001>.
  - [14] H.V. Grushevskaya, G. Krylov. Semimetals with Fermi Velocity Affected by Exchange Interactions: Two Dimensional Majorana Charge Carriers. *J. Nonlin. Phenom. in Complex Sys.* **18**, no. 2, 266-283 (2015).
  - [15] H.V. Grushevskaya, G. Krylov, V.A. Gaisyonok, D.V. Serow. Symmetry of Model N = 3 for Graphene with Charged Pseudo-Excitons. *Int. J. Nonlin. Phenom. in Complex Sys.* **18**, no. 1, 81-98 (2015).
  - [16] H.V. Grushevskaya, G.G. Krylov. Ch. 9. Electronic Structure and Transport in Graphene: QuasiRelativistic Dirac-Hartree-Fock Self-Consistent Field Approximation. In: *Graphene Science Handbook: Electrical and Optical Properties*. Vol. 3.

- Chapter 9. Eds. M. Aliofkhazraei *et al.* (Taylor and Francis Group, CRC Press, USA, UK, 2016). Pp.117-132.
- [17] H.V. Grushevskaya, G.G. Krylov. Massless Majorana-Like Charged Carriers in Two-Dimensional Semimetals. *Symmetry*. **8**,60 (2016).
  - [18] H. Grushevskaya, G. Krylov. Vortex Dynamics of Charge Carriers in the Quasi-Relativistic Graphene Model: High-Energy  $\vec{k} \cdot \vec{p}$  Approximation. *Symmetry*. **12**, 261 (2020).
  - [19] H.V. Grushevskaya, G.G. Krylov, S.P. Kruchinin, B. Vlahovic, S. Bellucci. Electronic properties and quasi-zero-energy states of graphene quantum dots. *Phys.Rev. B*. **103**, 235102 (2021).
  - [20] H. Grushevskaya, G. Krylov. Topologically Tuned Obliquity of Klein-Tunnelling Charged Currents Through Graphene Electrostatically-Confined p-n Junctions. *Int. J. Nonlinear Phenomena in Complex Systems*. **25**, 21-40 (2022).
  - [21] Y. Xu, X. Ye, L. Yang, P. He, Y. Fang. Impedance DNA biosensor using electropolymerized polypyrrole/multiwalled carbon nanotubes modified electrode. *Electroanalysis*. **18**(15), 1471-1478 (2006).
  - [22] T.I. Abdullin, O.V. Bondar', A.A. Rizvanov and I.I. Nikitina, "Carbon nanotube-based biosensors for DNA structure characterization," *Applied Biochemistry and Microbiology*, vol. 45(2), pp. 229-232, 2009.
  - [23] A. Benvidi, M.D. Tezerjani, Sh. Jahanbani, M.M. Ardakani and S.M. Moshtaghioun, "Comparison of impedimetric detection of DNA hybridization on the various biosensors based on modified glassy carbon electrodes with PANHS and nanomaterials of RGO and MWCNTs," *Talanta*, vol. 147, pp. 621-627, 2016.
  - [24] P. Abdul Rasheed and N. Sandhyarani, Carbon nanostructures as immobilization platform for DNA: A review on current progress in electrochemical DNA sensors. *Biosensors and Bioelectronics*. **97**, 226-237 (2017).
  - [25] K. Yoshikawa, M. Takahashi, V.V. Vasilevskaya, A.R. Khokhlov. Large discrete transition in a single DNA molecule appears continuous in the ensemble. *Phys. Rev. Lett.* **76**, 3029-3031 (1996).
  - [26] A.S. Babenko, H.V. Grushevskaya, N.G. Krylova, I.V. Lipnevich, V.P. Egorova, R.F. Chakukov. Nanopore-penetration sensing effects for target DNA sequencing via impedance difference between organometallic-complex-decorated carbon nanotubes with twisted single-stranded or double-stranded DNA. Chapter 17. In: *Advanced Nanomaterials for Detection of CBRN, NATO Science for Peace and Security*. Series A: Chemistry and Biology. J. Bonca and S. Kruchinin, Eds. (Springer, Dorchester, 2020). Pp. 247-258.
  - [27] H.V. Grushevskaya, N.G. Krylova, I.V. Lipnevich, A.S. Babenka, V.P. Egorova, R.F. Chakukov. CNT-based label-free electrochemical sensing of native DNA with allele single nucleotide polymorphism. *Semiconductors*. **52**(14), 1836-1838 (2018).
  - [28] H.V. Grushevskaya, I.V. Lipnevich, N.G. Krylova, A.S. Babenko. Electrochemical impedance spectroscopy sensing of viral DNA on surface of self-organized MWCNT-bundles decorated by organometallic complexes. In: *Proceedings of the XXVI Anniversary Seminar "Nonlinear phenomena in complex systems: Fractals, Chaos, Phase Transitions, Self-organization"*, Minsk, 21-24 May 2019. (Pravo i Ekonomika, Minsk, 2019). Pp. 65-70.
  - [29] V.P. Egorova, H.V. Grushevskaya, A.S. Babenka, R.F. Chakukov, N.G. Krylova, I.V. Lipnevich, E.V. Vaskovtsev. A single-molecule label-free identification of single-nucleotide colorectal-cancer-DNA polymorphism using impedance spectroscopy of self-redox-active decorated carbon nanotubes. *Semiconductors*. **54**(14), 1873-1876 (2020).
  - [30] H.V. Grushevskaya, I.V. Lipnevich, T.I. Orekhovskaya. Coordination Interaction between Rare Earth and/or Transition Metal Centers and Thiophene Series Oligomer Derivatives in Ultrathin Langmuir-Blodgett Films. *J. Modern Physics*. **4**, 7-17 (2013). <http://dx.doi.org/10.4236/jmp.2013.412A3002>
  - [31] H.V. Grushevskaya, N.G. Krylova, I.V. Lipnevich, V.P. Egorova, A.S. Babenka. Single nucleotide polymorphism genotyping using DNA sequencing on multiwalled carbon nanotubes monolayer by CNT-plasmon resonance.' *Int. J. Mod. Phys. B*. **32**, paper 1840033 (2018).
  - [32] H.V. Grushevskaya, N.G. Krylova, I.V. Lipnevich. Enhancement of Raman light scattering in dye-labeled cell membrane on metal-containing conducting polymer film. *Int. J. Mod. Phys.* **30**, paper 1642018 (2016).
  - [33] H.V. Grushevskaya, N.G. Krylova, I.V. Lipnevich, T.I. Orekhovskaja, B.G. Shulitski. Cell monolayer functioning detection based on quantum polarization effects in Langmuir-Blodgett multi-walled carbon nanotubes films. Chapter 8. In: *Nanomaterials for Security. NATO Science for Peace and Security*. Series A: Chemistry and Biology. J. Bonca and S. Kruchinin, Eds. (Springer, Dorchester, 2016). Pp. 89-99.
  - [34] I.I. Abramov, V.V. Hrushevski, G.G. Krylov, H.V. Krylova, I.V. Lipnevich, T.I. Orekhovskaja. A method of impedance calculation for impedimetric sensor with interdigital structure. *Petersburg electronics J.* **4**(73), 59-67 (2012).
  - [35] T. Araujo, P.B.C. Pesce, M.S. Dresselhaus, K. Sato, R. Saito, A. Jorio. Resonance Raman spectroscopy of the radial breathing modes in carbon nanotubes. *Physica. E* **42**, 1251-1261 (2010).
  - [36] V.Sh. Gangoli, Ju. Azhang, T.T. Willett, S.A. Gelwick, E.H. Haroz, Ju. Kono, R.H. Hauge, M.S. Wong. Using nonionic surfactants for production of semiconductor-type carbon nanotubes by gel-based affinity chromatography. *Nanomater. Nanotechnol.* **4**, 19 (2014). doi: 10.5772/58828
  - [37] V.D. Kraeft, D. Kremp, W. Ebeling, G. Röpke. *Quantum Statistics of Charged Particle Systems*. (Akademie, Berlin, 1986).
  - [38] H.V. Grushevskaya, N.G. Krylova, I.V. Lipnevich, T.I. Orekhovskaja, B.G. Shulitski. Electrochemical nanobiosensor for real-time detection of gap junction-mediated intercellular communication activity. *Advanced Materials Letters*. Vol. 8(4), 531-541 (2017). DOI: 10.5185/amlett.2016.7092
  - [39] A.S. Egorov, V.P. Egorova, H.V. Grushevskaya, N.G. Krylova, I.V. Lipnevich, T.I. Orekhovskaya, B.G. Shulitsky. CNT-enhanced Raman spectroscopy and its application: DNA detection and cell visualization. *Letters in Applied NanoBio-Science*. **5**(1), 346-353 (2016).